aerospace

MDPI

Article

Analysis and Optimization of the Wide-Speed-Range Aerodynamic Characteristics of SR-72-like Vehicles

Chao Feng [1,*], Fangzhou He [2], Bingchen Du [3], Gaojia Chen [1], Jun Li [1,*] and Lifang Zeng [1,4]

[1] School of Aeronautics and Astronautics, Zhejiang University, Hangzhou 310027, China; 17538826876@163.com (G.C.); lifang_zeng@zju.edu.cn (L.Z.)
[2] Huanjiang Laboratory, Zhuji 311800, China; qbxxfc@126.com
[3] Science and Technology on Space Physics Laboratory, China Academy of Launch Vehicle Technology, Beijing 100076, China; dbc0426@163.com
[4] Zhejiang Key Laboratory of Intelligent High Speed UAV Technology, Zhejiang University, Hangzhou 310027, China
* Correspondence: hyfengchao@zju.edu.cn (C.F.); lijun.uv@zju.edu.cn (J.L.)

Abstract

Recently, the United States unveiled a conceptual design of an unmanned high-speed vehicle, the SR-72, which boasts a maximum flight speed of Mach 6, enabling rapid airspace dominance and superior combat performance. To this end, this study conducted a comprehensive review of publicly available data and employed 3D modeling software to reconstruct the SR-72 configuration, utilizing the supersonic thin airfoil NACA 16006 for the wing design. Subsequently, a meticulously structured computational mesh was generated. Numerical simulations were conducted across subsonic, transonic, supersonic, and high-Mach-number flow regimes. The results reveal that the vehicle exhibits high maneuverability in subsonic conditions, with a stall angle of attack reaching 24°. In transonic conditions, significant wave drag is observed, while, in supersonic and high-Mach-number flow regimes at Mach 6, the vehicle demonstrates excellent wave-riding performance, enabling extended cruise durations and improved fuel efficiency. Furthermore, the initial airfoil was optimized using the CST (Class-Shape Transformation) parameterization method and the SLSQP (Sequential Least Squares Programming) algorithm. Under the given constraints, the drag coefficient was reduced by 40%, demonstrating a significant optimization effect.

Keywords: high speed vehicle; SR-72 UAV; numerical simulation; aerodynamic analysis

Academic Editors: Bosko Rasuo and Zhijin Wang

Received: 24 November 2025
Revised: 13 February 2026
Accepted: 14 February 2026
Published: 27 February 2026

1. Introduction

In today's era of technological advancement, aircrafts cruising at high Mach numbers have always been a hot topic of research in various countries.

Russia is a leading aerospace power globally. In Figure 1, the MiG-25 fighter jet, which broke flight records multiple times during the Soviet era [1,2], adopted a medium-sweep single wing, two side intakes, and a dual-engine, dual-vertical-tail aerodynamic layout, achieving a maximum flight speed of Mach 3. Later, the Rainbow D2 [3] and Eagle 31 programs [3] further advanced the pursuit of faster and higher wide-speed-range aircraft, reflecting the ongoing competition among major powers. In July 2016, officials from the Military Academy of the Russian Strategic Missile Force disclosed that Russia was actively researching high-speed stealth strategic bombers. The PAK-DA aircraft, with horizontal takeoff and landing capabilities, can reach any location worldwide within 1–2 h [4]. In 2018,

Russia announced that the development of the sixth-generation fighter jets, characterized by high-Mach capability, was actively progressing [5].

Figure 1. MiG-25 fighter jet [1,2].

The HyShot program, led by the University of Queensland in Australia, completed four flight tests and successfully demonstrated supersonic combustion in the engine. Japan's 2019 defense budget document outlines plans to develop high-speed-assisted gliding and high-speed cruise missile technologies through various projects. The annual budget for these projects amounts to 13.8 billion yen (approximately 840 million yuan). In fact, as early as 1986, Japan initiated the HOPE-X orbital spacecraft research project, which concluded in 2000 and yielded numerous key technologies for Japan's space science and technology. In 2002, Japan made significant advancements in supersonic engine technology and constructed a large high-Mach-number wind tunnel to study supersonic ramjet engines and high-speed aircraft. At the 2017 AIAA Conference in Xiamen, Japanese officials presented Japan's recent research projects on high-speed aircrafts, covering launch vehicles, reusable reentry vehicles (RBCC and TBCC), and advanced transport aircraft. Additionally, the Japan Aerospace Exploration Agency (JAXA) has long been researching next-generation high-speed vehicles. JAXA has initiated the NEXST, D-SEND, and S3TD programs to investigate low-drag, low-noise, and high-speed aircraft. JAXA collaborates with the SKY aviation agency to design small high-speed commercial aircraft.

The XB-70 high-altitude, high-speed strategic bomber, designed by North American Airlines in 1957, is depicted in Figure 2. The overall layout features a canard design, lacking a horizontal tail, with a large delta wing and a fully dynamic vertical tail, enabling fast horizontal takeoff and achieving a test flight speed of Mach 3 [6]. During high-speed flight, the downward deflection of the wingtip captures the two-dimensional oblique shockwave generated by the inlet at the fuselage belly, effectively preventing high-pressure airflow leakage. This creates a stable high-pressure zone on the lower surfaces of the fuselage and wings, enhancing the aircraft's lift-to-drag ratio. This represents an early application of the "wave riding" concept in aircraft design.

In the 1980s, the US Department of Defense and NASA initiated the National Aero-Space Plan (NASP) program [7], which proposed a test plan for the X-30 reusable spaceplane research aircraft. The aerodynamic configuration features a pointed front body and a large swept delta wing to minimize drag during high-speed flight. The latter half of the aircraft integrates the engines to enable horizontal runway takeoff and landing, as well as single-stage-to-orbit insertion. Due to the high costs and technological complexity, the X-30 project was suspended in 1993. However, its planning remains highly valuable for subsequent aerospace aircraft research. Subsequently, the Hyper-X project [8] was launched in 1996, encompassing the X-43A [9,10], X-43B, and X-43C. The X-43A is the world's first high-speed

aircraft powered by a scramjet engine. The successful test flight of the X-43A significantly advanced high-Mach-number flight technology research and development, sparking a global wave of high-speed aircraft research. The successful test flight of the X-43A marks the official transition of scramjet technology from the research stage to the engineering development stage [11].

Figure 2. XB-70 [6].

The US Air Force initiated a program concentrated on high-Mach-number technologies in 1995, named HyTech [12,13], aiming to advance scramjet technology for practical applications. The technology developed and accumulated in the HyTech program was later applied to the world-renowned X-51A flight test program [14–16], which achieved significant milestones in high-Mach-number flight. The X-51A aircraft adopted a wave riding layout for its precursor, and it achieved success in its fourth flight test [17,18] in May 2013, demonstrating the feasibility of high-Mach-number flight technology. The HyFly project [19], initiated by the Defense Advanced Research Projects Agency (DARPA) and the US Navy's Rapid Missile Response Validator, aimed to verify scramjet engine performance through flight tests, develop a high-speed cruise missile for time-sensitive targets, and adopt an axisymmetric missile design. The Falcon program [20,21], a collaboration between DARPA and the USAF, aims to develop and validate high-Mach-number flight technology for rapid global reach and demonstrate cost-effective space vehicles. This plan utilizes high-speed test aircraft, including HTV-1, HTV-2 [22–24] and HTV-3 (later developed as HTV-3X [25,26]), to conduct demonstration and verification experiments on various targets.

Research on high-Mach-number technology in China has been progressing steadily, with significant achievements made in recent years. In August 2018, the Aerodynamic Technology Research Institute of China Aerospace Science and Technology Corporation announced the successful launch of China's first "wave body" spacecraft, the Starry-2 rocket, which flew at Mach 6 for approximately 400 s. The successful launch of this rocket mission marked the completion of China's first domestic "wave body" flight test [27], a significant milestone in high-Mach-number technology development. In April 2019, the "Jiageng-1" wing reusable rocket, a collaborative project between Xiamen University and Beijing Lingkong Tianxing Technology Co., Ltd. (Beijing, China), was successfully launched [28]. The "Jiageng-1" has a total length of 8.7 m, a wingspan of 2.5 m, and a takeoff weight of approximately 3700 kg. The primary objective of this launch was to verify the aerodynamic characteristics of the high-speed twin ride wave front and the recyclability technology of the rocket. Numerous institutions in China, including the Chinese Academy of Sciences, National University of Defense Technology, and others, are actively engaged in high-speed vehicle research and have achieved significant milestones.

The United States has consistently prioritized the development of reconnaissance aircraft, resulting in the largest, most comprehensive, and most advanced types and models

in the world. As early as the 1960s and 1970s, the United States developed the SR-71 reconnaissance aircraft, which could fly at an altitude of 28,200 m and achieve a maximum Mach number of 3.6. The SR-71 Blackbird played a crucial role during the Cold War by infiltrating thousands of miles of Soviet and Chinese airspace to capture numerous intelligence photographs. The significant events it documented were promptly reported to the President of the United States. In 1988, the US military retired the SR-71 Blackbird due to unsustainable maintenance costs; however, it was reactivated a few years later in response to a tense global situation. Throughout its service, the SR-71 Blackbird completed only about 20% of its total assigned tasks, which amounted to over 3000 missions, excluding training operations. The SR-71 was constructed using the most advanced technology of its time and operated by highly skilled pilots. To this day, the SR-71 remains the fastest piloted aircraft in the world and holds two significant records.

Following the retirement of the SR-71 "Blackbird" due to various shortcomings, the United States has been eager to find a strategic replacement to continue global reconnaissance missions and has conducted relevant research. The SR-72 is one of the key initiatives.

The SR-72 reconnaissance aircraft was developed by Lockheed Martin Corporation [29–31]. This aircraft model encompasses a complete reconnaissance system, takes off from conventional runways, and is capable of carrying advanced weapons in ultra-high to critical airspace. It is anticipated to achieve a maximum Mach number of 6. The public diagram reveals that the SR-72 features a front-mounted body, a high spine, a large-aspect-ratio fuselage, a thin trapezoidal wing with a large sweep and small aspect ratio, and a wing–body fusion, single-vertical-tail layout, all of which meet the aerodynamic performance requirements from subsonic to high-Mach-number flows. The integrated design of the engine inlet and fuselage facilitates the pre-compression of high-Mach-number inflow.

Lockheed Martin and Aerojet Rocketdyne will divide the development and testing of the future SR-72 into two phases. In the first phase, a manned flight research vehicle (FRV) is set to be developed, with plans to commence in 2018 and achieve its maiden flight in 2023. Its design parameters include being equivalent in size to the F-22, approximately 18.3 m long, powered by a single scramjet engine, and capable of flying at Mach 6 for several minutes to complete preliminary verification. The second phase will initiate the design research of the SR-72 high-speed aircraft, which is expected to be completed and operational by 2030.

Guo Yuchen from Nanjing University of Aeronautics and Astronautics [32] analyzed the basic aerodynamic characteristics and heat transfer of the SR-72 drone in his Master's thesis; however, the mesh used was not sufficiently precise. This article presents a high-quality grid structure partitioning for the model, featuring a grid size of 8 million, which results in more accurate calculation outcomes.

The simulation calculation of high-speed aircraft is also full of challenges. Due to the high Mach number, the flow field near the shockwave is difficult to calculate, and there are high requirements for grid drawing and computer performance. In addition, there are requirements for the selection of parameterization and optimization methods in the optimization of aircraft airfoils.

This paper selects the SR-72 unmanned aircraft as the research subject. First, a three-dimensional model was reconstructed based on publicly available online data. Subsequently, computational fluid dynamics (CFD) analysis was conducted using the FLUENT software to numerically simulate the aerodynamic performance across four distinct speed regimes: subsonic, transonic, supersonic, and high-Mach-number flows. The variations

in key aerodynamic parameters, including lift coefficient, drag coefficient, and flow field structures, were systematically analyzed under these different speed conditions.

Finally, an aerodynamic optimization study was performed specifically for the airfoil under high-Mach-number conditions. An optimization framework was established for the NACA 16006 airfoil, employing the Class-Shape Transformation (CST) method for 5th-order parametric representation. The optimization process incorporated constraints on lift coefficient, wing area, and pitching moment coefficient, with the objective function set to minimize drag. The optimized aerodynamic configuration was successfully derived, demonstrating improved performance.

2. Methods

2.1. Aerodynamic Equations

The Navier–Stokes (N-S) [33] equations describe fluid motion, adhering to three fundamental laws of conservation in physics: the conservations of mass, momentum, and energy. The equations are as follows:

Continuity equation:

$$\frac{\partial \rho}{\partial t} + \nabla \cdot (\rho \vec{V}) = 0 \tag{1}$$

Momentum equation:

$$\rho \frac{\partial \vec{V}}{\partial t} + \rho(\vec{V} \cdot \nabla)\vec{V} = \rho \vec{f} - \nabla p + \nabla(\lambda \nabla \cdot \vec{V}) + \nabla \cdot \mu[\varepsilon] \tag{2}$$

Energy equation:

$$\rho \frac{\partial h}{\partial t} + \rho(\vec{V} \cdot \nabla)h = \frac{\partial p}{\partial t} + (\vec{V} \cdot \nabla)p + \Phi + \nabla \cdot (k \nabla T) \tag{3}$$

The above represents the N-S equation system, commonly used for solving flow problems. In cases of small changes in flow parameters, the viscosity term in the N-S equations can be neglected, leading to the Euler equation system. In a steady state, the time term and total force can also be ignored, simplifying the Euler equations as follows:

$$\nabla \cdot (\rho \vec{V}) = 0 \tag{4}$$

$$\rho(\vec{V} \cdot \nabla)\vec{V} = -\nabla p \tag{5}$$

In the present computational simulations, the single-equation Spalart–Allmaras (S-A) turbulence model was employed. This model has the following limitations: it cannot accurately capture complex turbulence mechanisms; and its performance degrades in shock–boundary-layer interactions and under strong compressibility effects, which may require compressibility corrections or more advanced turbulence models. At high Mach numbers, aerodynamic heating (aerothermal effects) must also be taken into account, including the potential for chemical reactions in the gas at elevated temperatures. Furthermore, the present study is limited to aerodynamic characteristics; flight trim and controllability were not addressed, and future work should include a more comprehensive whole-aircraft assessment. The Spalart–Allmaras (S-A) model is represented by the following equation:

$$\frac{\partial}{\partial t}(\rho \tilde{\nu}) + \frac{\partial}{\partial x_i}(\rho \tilde{\nu} u_i) = G_\nu + \frac{1}{\sigma_{\tilde{\nu}}}\left\{ \frac{\partial}{\partial x_i}\left[(\mu + \rho \tilde{\nu}) \frac{\partial \tilde{\nu}}{\partial x_j} \right] + C_{b2\rho}\left(\frac{\partial \tilde{\nu}}{\partial x_i} \right)^2 \right\} - Y_\nu + S_{\tilde{\nu}} \tag{6}$$

The finite volume method is employed to decompose the entire computational domain into several control volumes, applying conservation-type control equations to each volume to obtain a set of discrete equations. The flux of the boundary integral is approximately calculated using the flow parameters of the control volumes on both sides. The finite volume method divides the computational domain into a series of non-repeating control volumes, assuming that each volume remains constant over time. Therefore:

$$\frac{\partial \vec{W}}{dt} = -\frac{1}{\Omega}\int_{\partial\Omega} (\vec{Q}_c - \vec{Q}_v) dS \tag{7}$$

For any unit cell Ω_i, the area on the right-hand side of the equation can be approximated as the sum of the fluxes flowing out of its boundary. Thus, we can derive:

$$\frac{\partial \vec{W}}{dt} = -\frac{1}{\Omega_i}\left[\left(\sum_{m=1}^{N_F} (\vec{Q}_c)_m \cdot \Delta S_m\right) - \left(\sum_{m=1}^{N_F} (\vec{Q}_v)_m \cdot \Delta S_m\right)\right] \tag{8}$$

Here, N_F represents the total number of faces on the control volume Ω_i, and ΔS_m is the area of face m. Each control volume can establish the above equation, and the differential equation to be solved can be integrated for each volume to obtain a set of discrete equations.

2.2. Validity Verification of Numerical Simulation

A simulation of a cylinder at high speed was conducted, with the calculation grid illustrated in Figure 3. The calculation parameters are as follows: Mach number 8.03, Reynolds number 1.835×10^5, static temperature 124.94 K, wall temperature 294.44 K, and static pressure 840 Pa. The inlet of the computational domain is designated as inflow, the outlet as extrapolation, and the wall as isothermal. The experimental data is sourced from the literature [34], conducted in a 48-foot ultra-high-speed shockwave wind tunnel at the Calspan UB Research Center. The model is a stainless-steel cylinder with a diameter of 3 inches and a length of 24 inches. A comparison diagram of pressure distribution on the cylindrical surfaces is shown in Figure 4. The surface pressure was normalized using a stationary point value of P_0 = 72,188.1372 Pa.

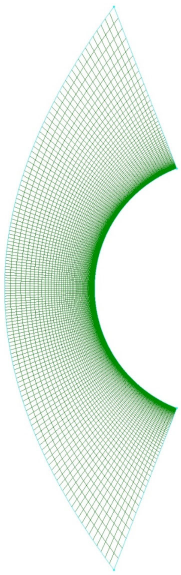

Figure 3. Schematic diagram of cylindrical grid.

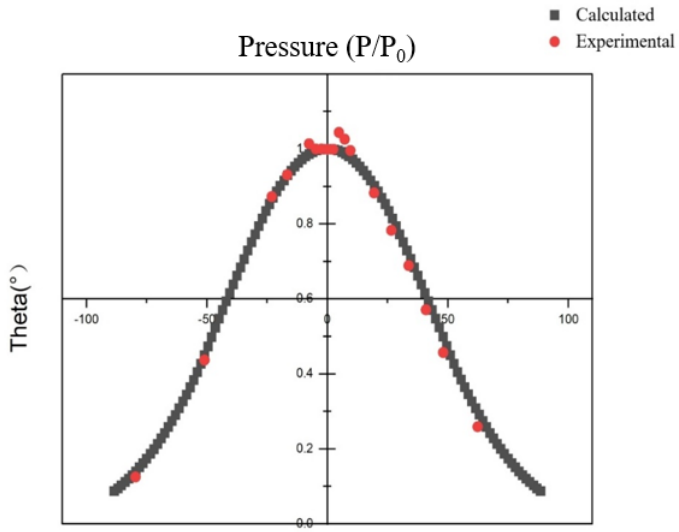

Figure 4. Calculation and experimental comparison of cylindrical circular pressure coefficient (Ma = 8.03).

2.3. Grid Independence Verification

To verify grid convergence, three distinct grid systems were generated and evaluated under the high-Mach-number flow conditions of Mach 6 with a 6° angle of attack for validation. The computational results obtained from these three grid resolutions are systematically compared in Table 1. Table 2 further compiles the critical convergence metrics (including residual histories, iterative stability parameters, and characteristic solution discrepancies) for each grid configuration, providing quantitative evidence of spatial discretization independence, where $p = \ln[(f_3 - f_2)/(f_2 - f_1)]/\ln(r)$ is the estimated global order of convergence on coefficient f, $f_{exact} = f_1 + (f_1 - f_2)/(r^p - 1)$ is the Richardson extrapolated value of the coefficient at zero mesh size 35, and $\mathrm{GCI}_{i+1,i} = F_s(|f_{i+1} - f_i|)/(f_i(r^p - 1))$ is the Grid Convergence Index defined by Roache [35]. The safety factor Fs is assumed to be 1.25, and a small value of GCI indicates that the computation is within the asymptotic range. As evidenced by the data, the Geometric Conservation Law (GCL) metric for Grid 12 registers below 0.1%, thereby confirming that the spatial resolution and element count of Grid 2 satisfy the prescribed numerical accuracy criteria for high-Mach-number flow simulations.

Table 1. Grid sizes and results of the convergence study.

Grid Level	Mesh Size	Cells	C_L	C_D
3	189 × 92 × 69	1,198,000	0.0125	0.0875
2	379 × 185 × 139	9,175,500	0.5098	0.1045
1	757 × 369 × 277	77,350,000	0.5223	0.1056

Table 2. Order of accuracy and grid convergence index estimation.

Parameter	p	f_{exact}	GCL_{32}%	GCL_{21}%
C_L	5.3141	0.5226	3.14	0.07
C_D	3.9499	0.1057	1.41	0.09

2.4. SR-72 UAV Model Establishment and Computing Environment Setting

According to various public sources, the SR-72 drone is characterized by a high back, a large-aspect-ratio fuselage, wing–body fusion, large swept delta wings, and twin-engine air intakes. The model diagram is created using 2012 version of Solid Works,

as shown in Figure 5. To meet the aerodynamic requirements of high-speed flight, the symmetrical thin airfoil NACA 16006 was selected for its favorable high-speed performance characteristics. Subsequently, a shape optimization study was conducted to further enhance its aerodynamic efficiency under high-Mach-number flow conditions.

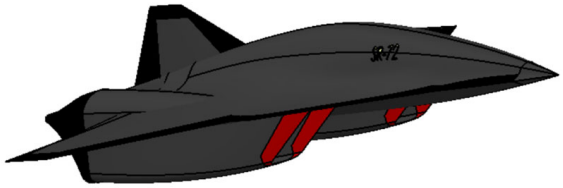

Figure 5. SR-72 3D modeling diagram.

Due to only considering the aerodynamic characteristics of the aircraft, the engine and vertical tail were simplified during grid partitioning. Structured grids are utilized in the calculations, facilitating boundary fitting within the region. The grid generation speed is rapid, the quality is high, and the structure is straightforward. The aircraft is symmetrical on both sides, and lateral characteristics are not considered in this analysis. This article focuses on modeling only half of the aircraft to reduce the total number of grids. When dividing the boundary layer of the model into grids, Y+ was set to 1, resulting in a first layer grid thickness of 1.6834×10^{-5} m, with a total of 35 grid layers and approximately 9.3 million grids. The total length of the aircraft is 13 m, while the calculation domain length is approximately 260 m. The length of the calculation domain was set to 10 times the length of the fuselage at both the front and rear. The schematic diagram after grid division is shown in the Figure 6, which is a schematic diagram of the overall grid of the aircraft.

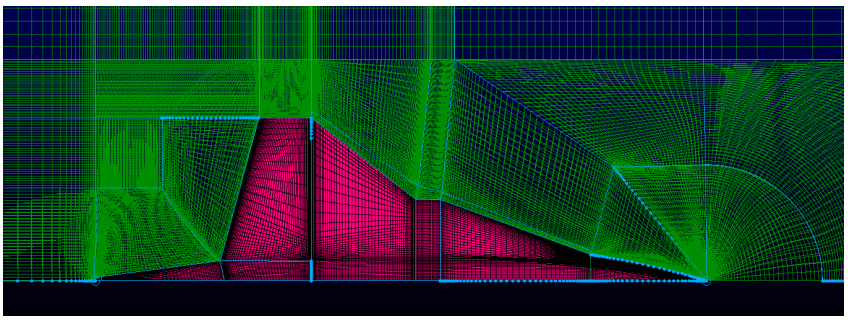

Figure 6. Aircraft whole-machine calculation grid.

The boundary conditions for the simulation were established as follows:

(1) Symmetric boundary condition: The tangent plane of the half model was defined as a symmetric plane, with both normal velocity and normal gradient set to 0;

(2) Boundary condition for the object surface: The surface of the aircraft was defined as the object surface boundary, ensuring that the surface airflow was non-slip and non-penetrable;

(3) Far-field boundary conditions: Given that the gas properties involve compressible flow, the other surfaces were defined as pressure far-field, and aerodynamic calculations were conducted by specifying the Mach number and direction of the gas flow.

The calculation model employed a single-equation S-A model, which effectively simulated a wide range of flow field motions. The implicit coupling solution method and a density-based solver were utilized. The main calculation parameters discussed in this article are presented in Table 3, below:

Table 3. Calculation parameters.

Calculation Parameters	Subsonic	Transonic	Supersonic	High Mach Number
Height (H/m)	0	10,000	30,000	30,000
Pressure (P/Pa)	101,325	26,500	2330.5	2330.5
Sound of speed (m/s)	340	299.5	301.75	301.75
Mach number (Ma)	0.3, 0.4, 0.5	0.9, 1.1	2, 3	6
Temperature (T/K)	288	223.3	226.5	226.5

2.5. CST Parameterization Method

When optimizing an airfoil, it is necessary to first convert the geometric information of the airfoil into algebraic parameters to facilitate iterative optimization processes. In this study, the CST parameterization method was employed, which was initially proposed by Kulfan [36]. The method combines a class function $C(x)$ and a shape function $S(x)$, multiplied together, with an additional trailing-edge thickness function. The mathematical formulation is as follows:

$$y(x) = C(x) \cdot S(x) + x \cdot \Delta y_{te} \tag{9}$$

$C(x) = x^{N1}(1-x)^{N2}$ is used to control the overall category of the airfoil. Different wing shapes have different values for $N1$ and $N2$. $S(x)$ is used to describe the changes in local curvature of an airfoil. Δy_{te} is an adjustment of the thickness of the trailing edge of the airfoil.

When performing parameterization, using a lower order often fails to clearly represent the shape, while using a higher order can lead to an increased computational burden. After reviewing the literature, this study adopted a fifth-order CST parameterization representation.

3. Aerodynamic Characteristic Analysis of SR-72 Unmanned Aerial Vehicle

3.1. Analysis of Low-Speed Characteristics of SR-72 Unmanned Aerial Vehicle

The following, Figures 7 and 8, illustrate the aerodynamic parameters, including the lift coefficient and drag coefficient, of the SR-72 drone within the low-acoustic-velocity range. A total of three Mach numbers, 0.3, 0.4, and 0.5, were calculated. Curve analysis indicates that, as the Mach number increases, the lift coefficient also continues to rise. The lift coefficient reaches its maximum at an angle of attack of 24°, after which the aircraft stalls. It can be reflected in the flow field diagram of the aircraft. Similarly, the drag coefficient also increases as the angle of attack rises, demonstrating an upward trend with increasing Mach number. The lift-to-drag ratio curve indicates that, at subsonic speeds, the lift-to-drag ratios for the three Mach numbers are nearly identical, showing minimal influence from the Mach number. The lift-to-drag ratio reaches its maximum at an angle of attack of 4°.

In the low-speed sound domain, as the aircraft flies, the air bypasses the leading edge of the wing and flows over the upper surface of the fuselage for a greater distance than over the lower surface, resulting in negative pressure. As the angle of attack increases, the airflow at the leading edge of the wing generates detached vortices, leading to a loss of suction on the upper surface's leading edge and an increase in induced drag. As resistance increases, the detached vortices can generate vortex lift at high angles of attack, which increases the stall angle and enhances the drone's maneuverability. Additionally, the detached vortices generated on the wing's surface can increase surface suction, thereby improving aircraft lift. In Figures 9 and 10, based on the analysis of the pressure flow field cloud maps, flow field cloud maps at Mach number 0.5 for angles of attack of 0°, 4°, 10°, and 14° were selected. At an angle of attack of 0°, the pressure distribution on the upper surface of the fuselage is relatively uniform. As the angle of attack increases, a negative

pressure zone gradually develops near the wing strips, generating leading edge suction. At an angle of attack of 10°, a distinct transverse negative pressure zone forms between the wing strips and the leading edge, gradually expanding toward the trailing edge. At an angle of attack of 14°, a stable negative pressure zone is observed on the upper surface of the wing, where detached vortices form, providing significant vortex lift and enhancing aircraft maneuverability.

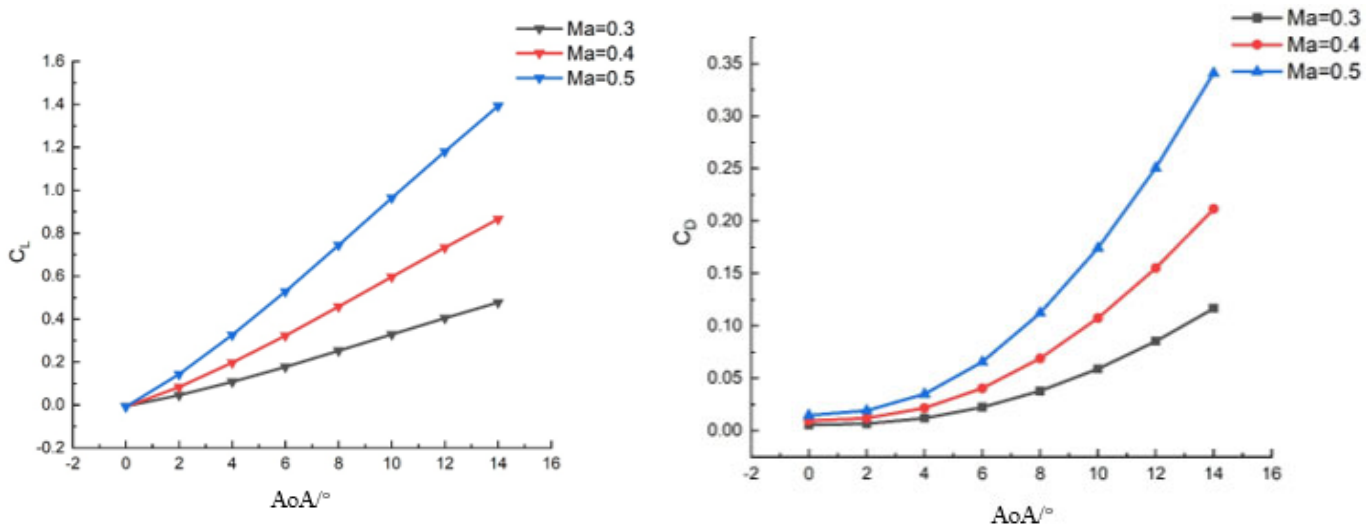

Figure 7. Subsonic lift coefficient curve (**left**) and drag coefficient curve (**right**).

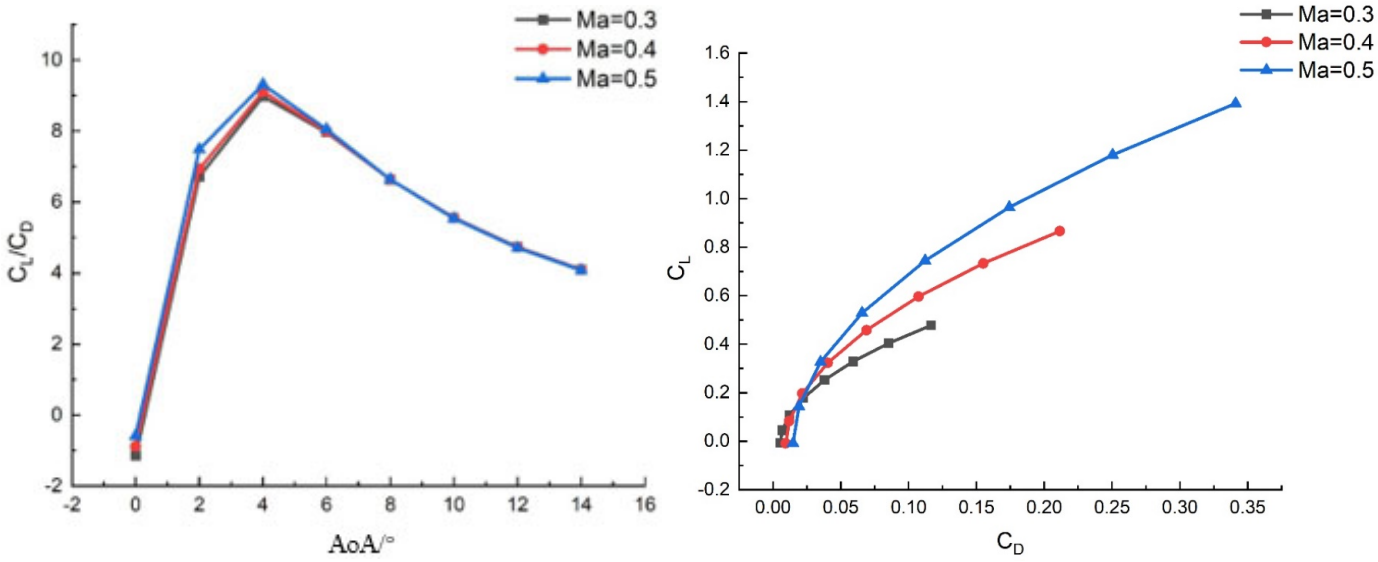

Figure 8. Subsonic lift-to-drag ratio curve (**left**) and polar curve (**right**).

In the left diagram of Figure 11, aerodynamic analysis reveals that, at a 24° angle of attack, the upper fuselage exhibits extensive negative pressure zones, accompanied by a significant pressure differential between the upper and lower surfaces, resulting in an elevated lift coefficient. In the right diagram of Figure 11, where the angle of attack increases to 30°, the pressure coefficient contour plots demonstrate that the low-pressure region becomes highly localized near the canard–root junction. At this critical angle, flow separation occurs as the boundary layer detaches from the airframe, thereby suppressing further lift enhancement. The stagnation of lift coefficient growth beyond 30° conclusively identifies the onset of aerodynamic stall. This nonlinear lift degradation mechanism

confirms that the unmanned aerial vehicle enters a fully developed stall regime within the 24–30° angle of attack range.

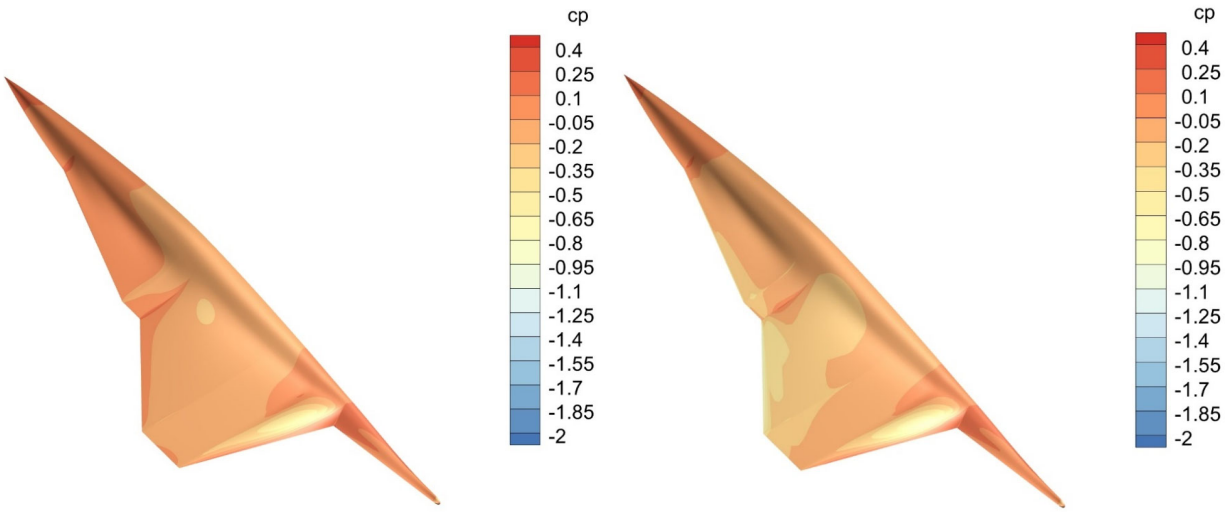

Figure 9. Mach number 0.5; pressure coefficient on the upper surface of the fuselage (AoA = 0° (**left**) and AoA = 4° (**right**)).

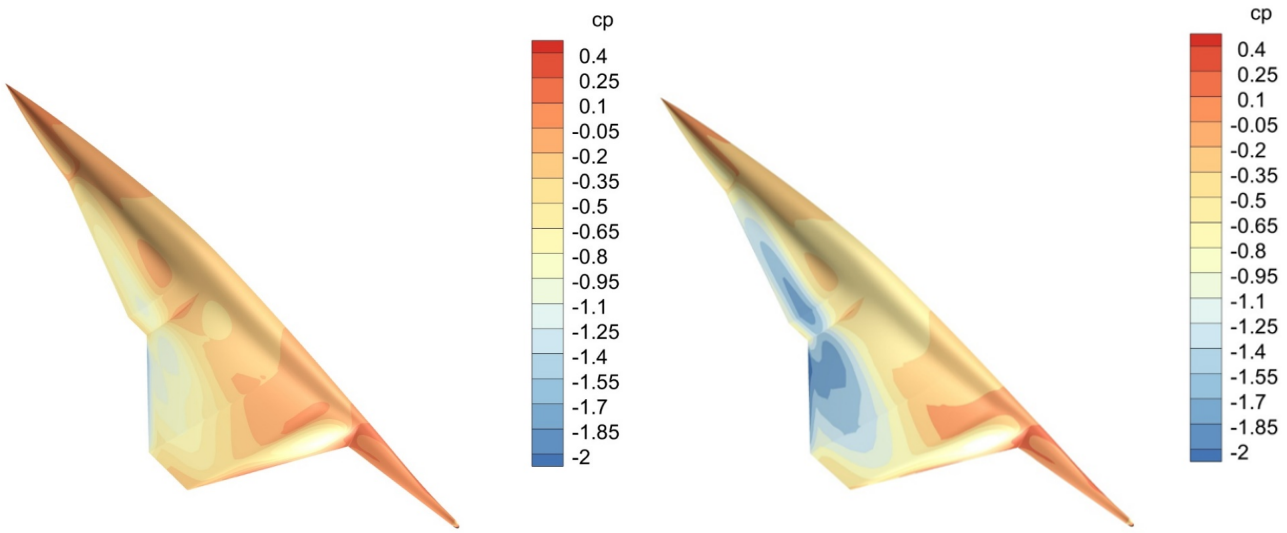

Figure 10. Mach number 0.5; pressure coefficient on the upper surface of the fuselage (AoA = 10° (**left**) and AoA = 14° (**right**)).

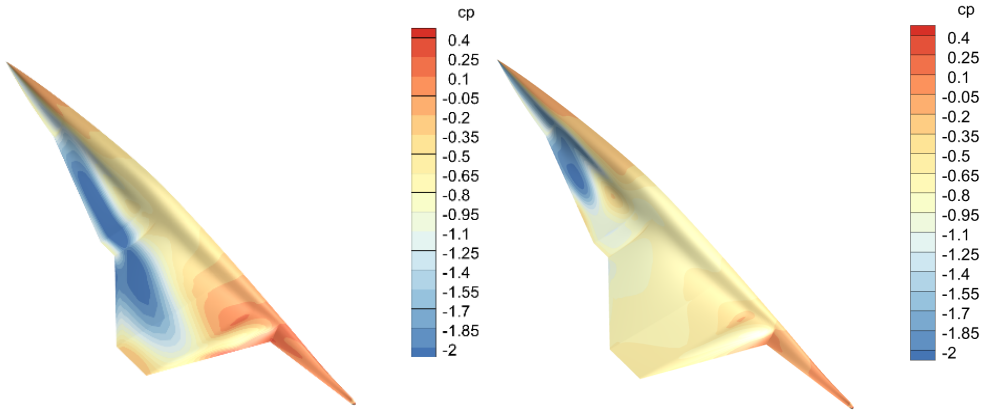

Figure 11. Mach number 0.5; pressure coefficient on the upper surface of the fuselage (AoA = 24° (**left**) and AoA = 30° (**right**)).

3.2. Analysis of Transonic-Speed Characteristics of SR-72 Unmanned Aerial Vehicle

In the transonic range, Mach numbers 0.9 and 1.1 were analyzed. The aerodynamic coefficient diagram (Figure 12) shows that the lift coefficient increases with the angle of attack, while the drag coefficient also rises significantly. As shown in Figure 13, at Mach 1.1, the maximum lift-to-drag ratio is notably lower than at Mach 0.9, as local shockwaves near the critical Mach number reduce aerodynamic efficiency.

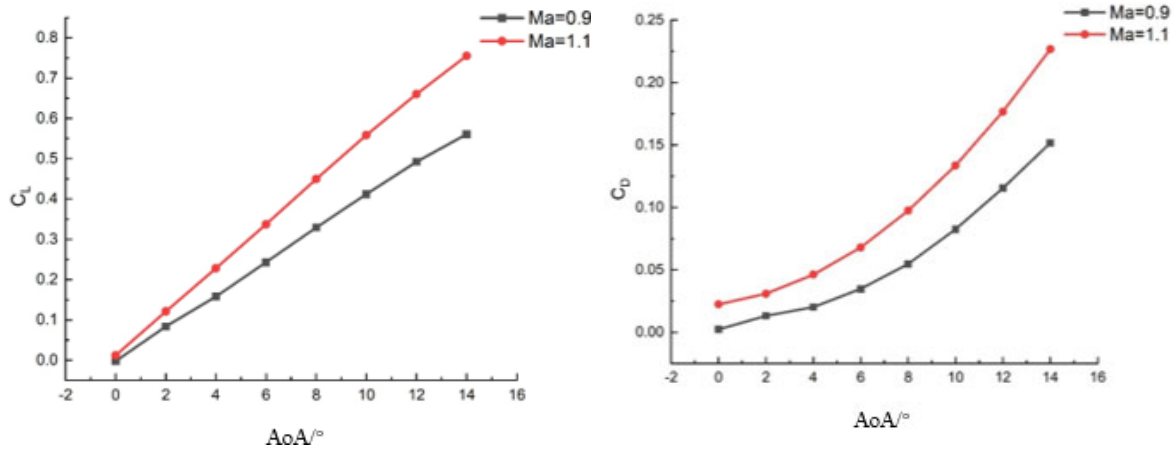

Figure 12. Transonic lift coefficient curve (**left**) and drag coefficient curve (**right**).

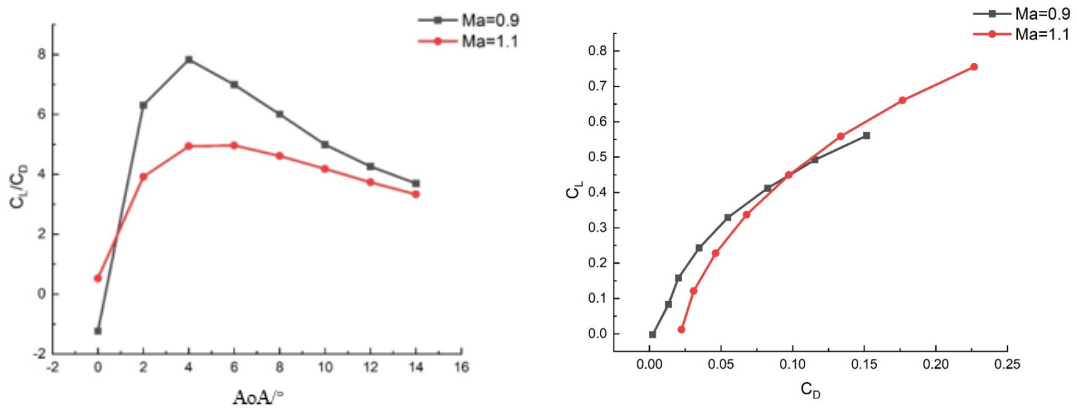

Figure 13. Transonic lift-to-drag ratio curve (**left**) and polar curve (**right**).

The pressure coefficient cloud map reveals significant negative pressure at the trailing edge and main wing edge on the upper fuselage at 0° angle of attack, caused by shockwaves reducing surface air pressure. As the angle of attack increases, the negative pressure zone expands into the fuselage, while the lower surface experiences high pressure at the main wing edge, contributing to significant wave drag (Figures 14 and 15). In the supersonic phase, different parts of the aircraft approach the critical Mach number, causing complex changes in the flow field and potential flight instability, requiring careful attention from designers.

3.3. Analysis of Supersonic-Speed Characteristics of SR-72 Unmanned Aerial Vehicle

In the supersonic stage, Mach 2 and Mach 3 were analyzed. The changes in aerodynamic parameters are shown in Figures 16 and 17. The lift-to-drag ratio curve shows that Mach 3 achieves a slightly higher peak ratio (4.6) compared to Mach 2 (4.5) across all angles of attack. At higher Mach numbers, airflow compression and shockwaves enhance lift efficiency. However, the steeper descent curve for Mach 3 indicates greater sensitivity to angle of attack changes and more pronounced flow separation. These characteristics

can inform optimizations in aircraft design and flight strategies to enhance performance and efficiency.

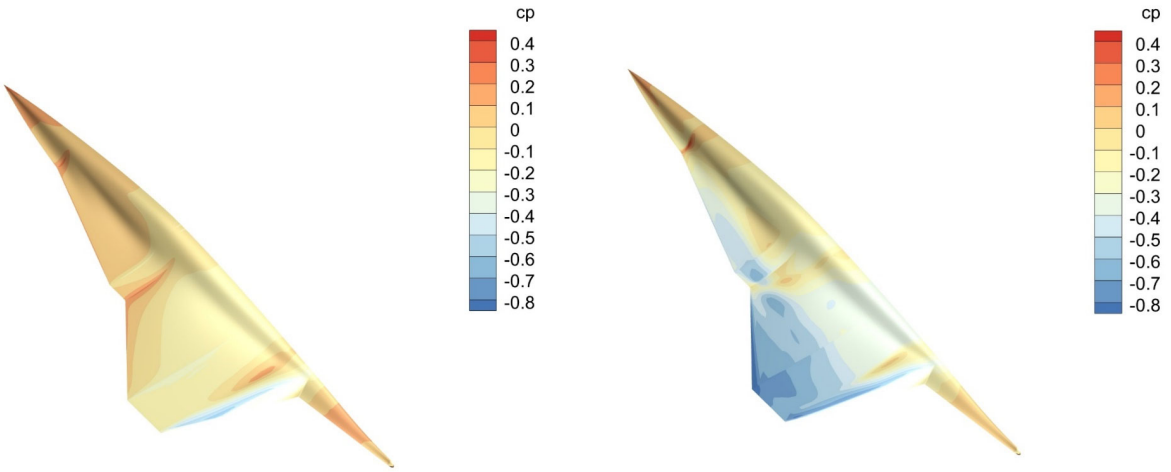

Figure 14. Mach number 1.1; pressure coefficient on the upper surface of the fuselage (AoA = 0° (**left**) and AoA = 4° (**right**)).

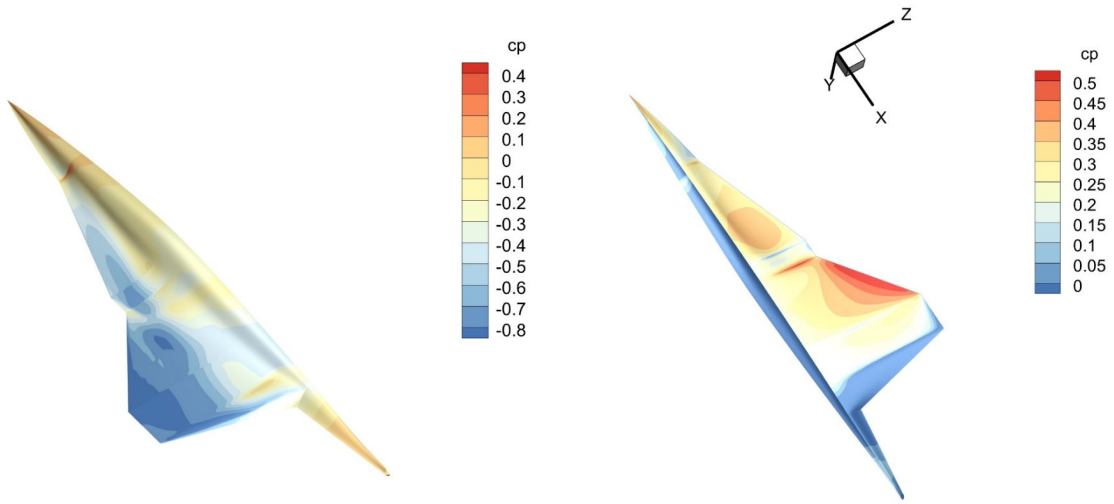

Figure 15. Mach number 1.1; angle of attack 14°; pressure coefficient on the upper (**left**) and lower (**right**) surfaces of the fuselage.

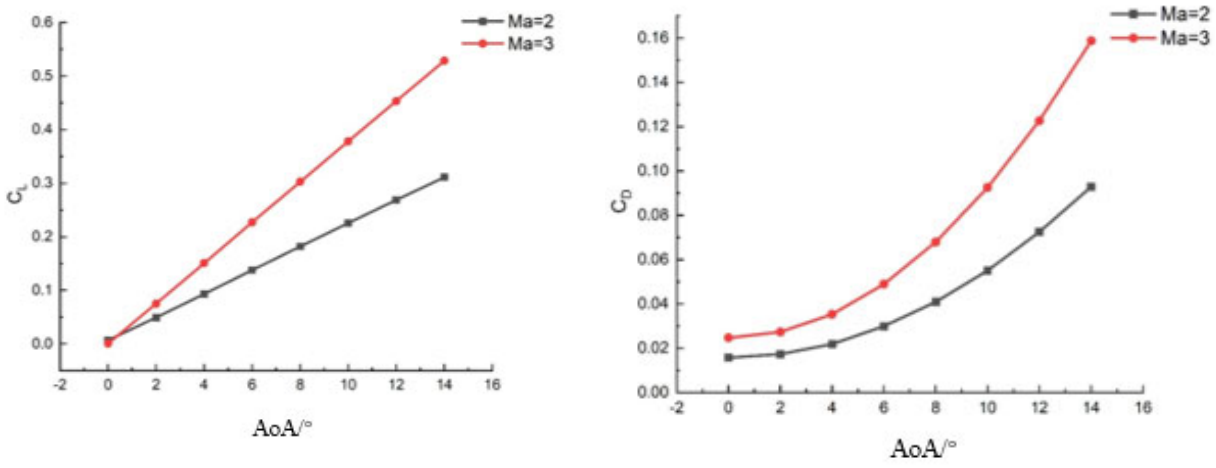

Figure 16. Supersonic lift coefficient curve (**left**) and drag coefficient curve (**right**).

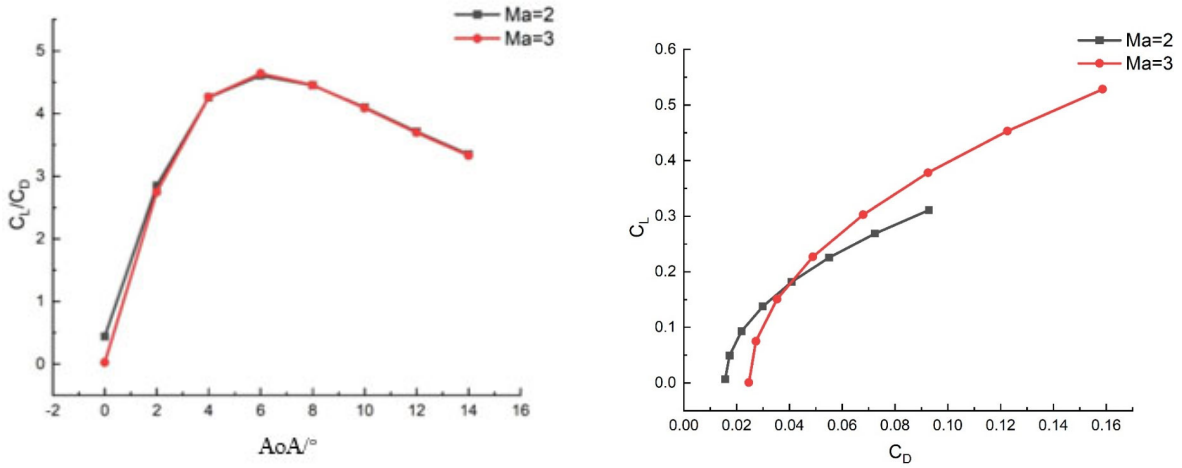

Figure 17. Supersonic lift-to-drag ratio curve (**left**) and polar curve (**right**).

Figure 18(left) depicts the flow field at Mach 3 and 0° angle of attack. At the wing's leading edge, airflow decelerates and compresses, forming a shockwave and creating a high-pressure zone. On the upper wing surface, airflow accelerates, reducing pressure due to expansion waves. At the trailing edge, airflow recompresses, creating a high-pressure zone, where flow separation leads to eddies or turbulence. Analysis of pressure coefficient distribution can guide wing design optimizations to minimize shock drag and flow separation, enhancing overall performance.

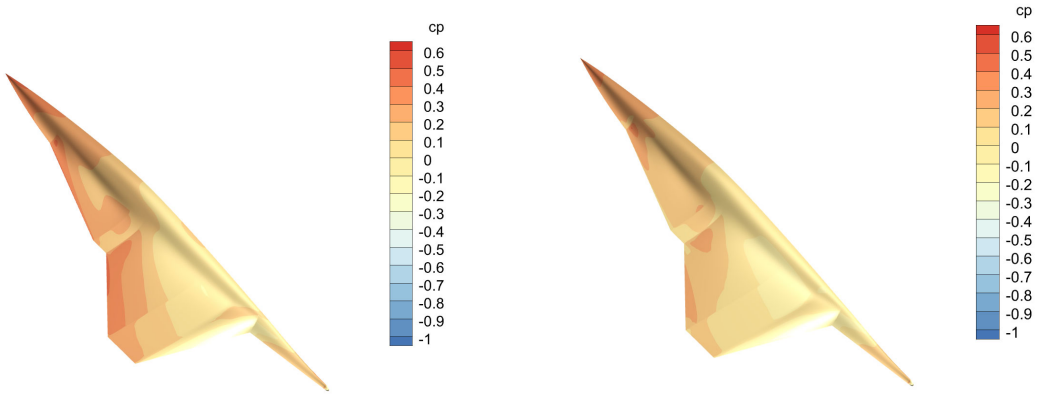

Figure 18. Mach number 3; pressure coefficient on the upper surface of the fuselage (AoA = 0° (**left**) and AoA = 4° (**right**)).

3.4. Analysis of High-Mach-Number Characteristics of SR-72 Unmanned Aerial Vehicle

Based on public information, the SR-72 can reach Mach 6, which was included in the simulation analysis. The aerodynamic parameters of the aircraft at Mach 6 are shown in Figures 19 and 20. The aerodynamic coefficient curve shows a linear increase in lift coefficient with angle of attack, indicating heightened sensitivity under high-Mach-number conditions. Designers must carefully control the angle of attack to prevent stall or instability. The linear rise in drag coefficient at high angles significantly impacts flight efficiency and fuel consumption. The lift-to-drag ratio peaks at a 6° angle of attack, marking optimal efficiency. Beyond this, the ratio declines, with aerodynamic characteristics being highly sensitive to angle of attack changes under supersonic conditions.

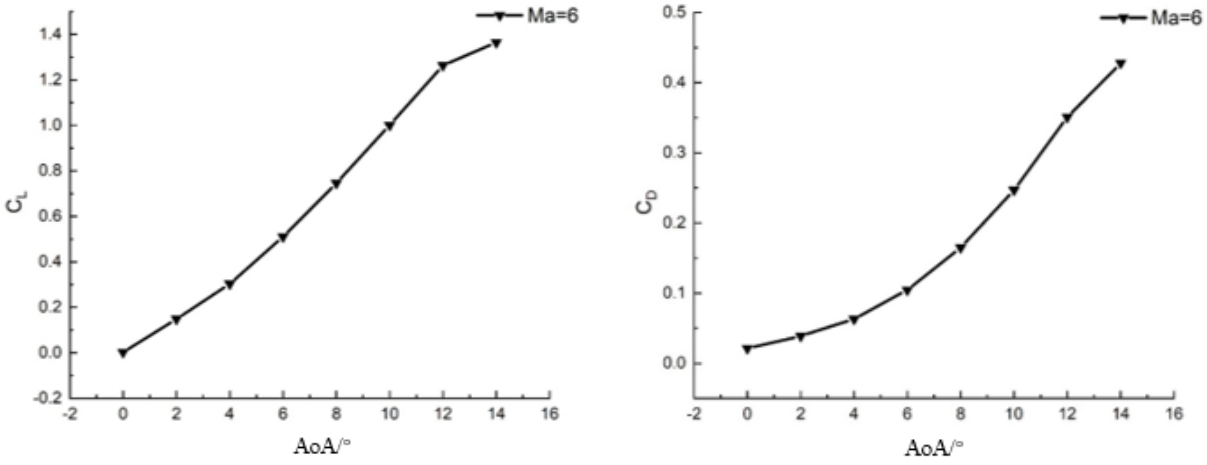

Figure 19. Lift coefficient curve (**left**) and drag coefficient curve (**right**) at Mach number 6.

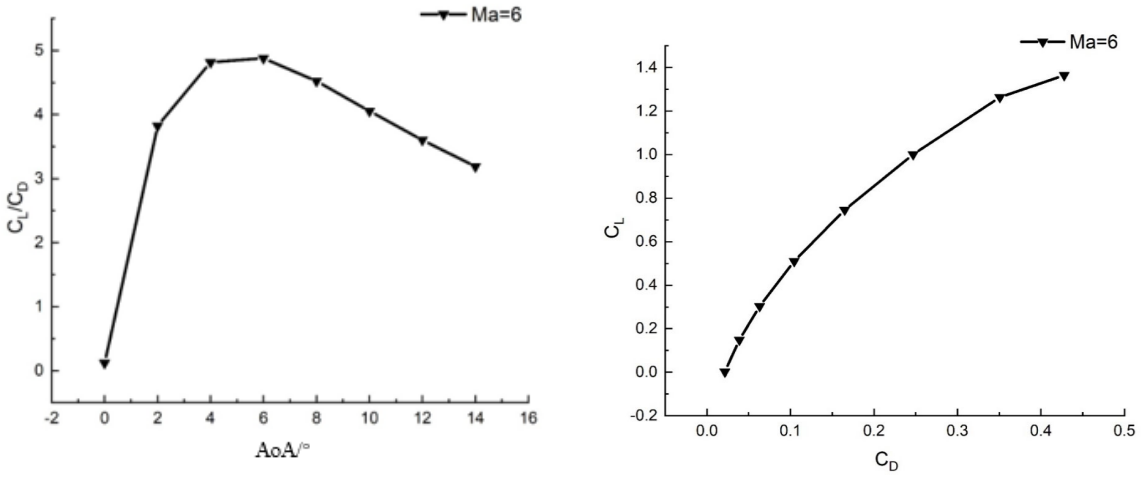

Figure 20. Lift-to-drag ratio curve (**left**) and polar curve (**right**) at Mach number 6.

Figure 21 illustrates the pressure coefficient distribution at Mach 6 and 0° angle of attack. High pressure in the nose section generates a strong bow shockwave, reducing air velocity and increasing pressure downstream. The pressure coefficient chart at the fuselage bottom shows shockwaves at the wing's leading edge (Figure 22). At the tail and trailing edge, the pressure coefficient is lower, with expansion waves forming due to geometric changes, creating a low-pressure zone.

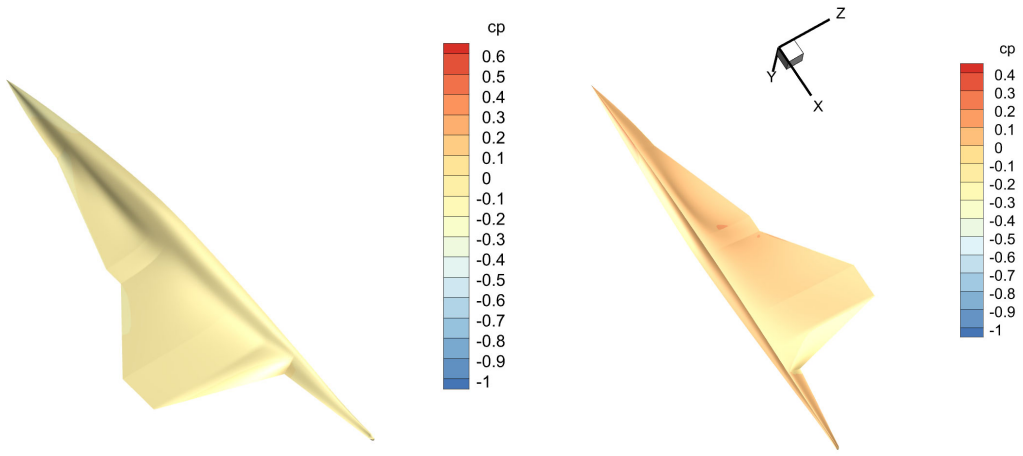

Figure 21. Pressure coefficient on the upper (**left**) and lower (**right**) surfaces of the fuselage at Mach 6 with angle of attack 0°.

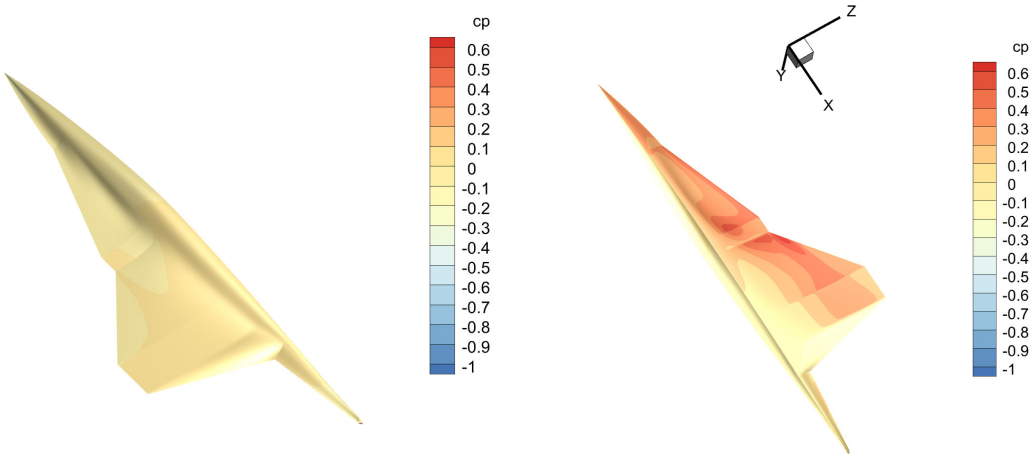

Figure 22. Pressure coefficient on the upper (**left**) and lower (**right**) surfaces of the fuselage at Mach 6 with angle of attack 10°.

4. Optimization and Analysis of NACA 16006 Airfoil

For the NACA 16006 airfoil employed on the SR-72 vehicle in this study, an optimization framework was established. Starting with geometric parameterization, the computational mesh was initialized, followed by flow field computation in fluent. The Sequential Least Squares Programming (SLSQP) method was utilized for iterative optimization, with convergence determined by evaluating the objective and constraint functions. The optimization loop terminates upon convergence, and the framework is illustrated in the accompanying Figure 23. The optimization conditions were set at Mach 6 and an angle of attack of 6 degrees.

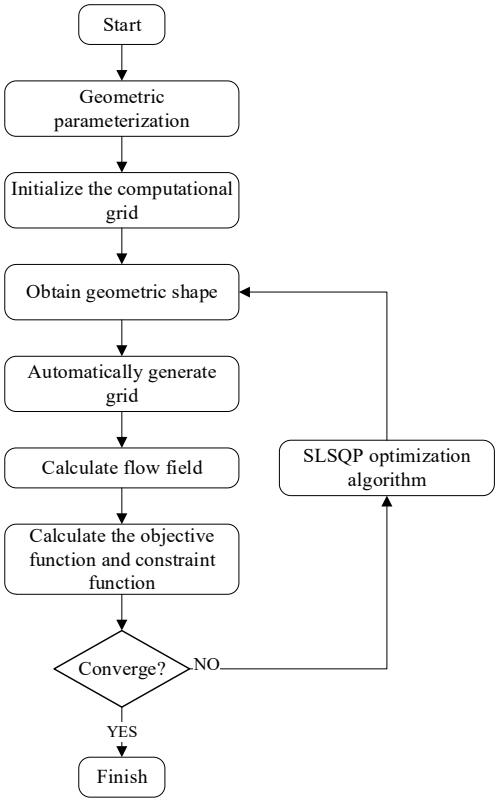

Figure 23. Optimization framework diagram.

The problem can be mathematically summarized as:

$$\begin{aligned} &\text{Minimize } C_D \\ &\text{s.t. } C_L = 0.0819 \\ &C_M \geq -0.0118 \\ &\text{A} \geq A_{baseline} \end{aligned}$$

A comparative analysis of the flow field for the optimized airfoil configuration is presented in the figures. After 232 iterations, the drag coefficient shows a significant reduction, and all constraints are satisfied. In Figures 24–26, left panels display the distributions of pressure coefficient, temperature, and density variations for the baseline configuration, while the right panels illustrate the corresponding results for the optimized configuration. The analysis reveals that the baseline configuration exhibits notable drag at the leading edge and unstable flow characterized by a sharp pressure coefficient drop at the mid–rear region. In contrast, the optimized airfoil demonstrates a smoother pressure gradient on the upper surface, reduced flow separation, and enhanced flow stability. The optimized flow field exhibits cleaner streamline patterns with reduced temperature near the airfoil surface, contributing to a higher lift-to-drag ratio due to the increased pressure differential between the upper and lower surfaces.

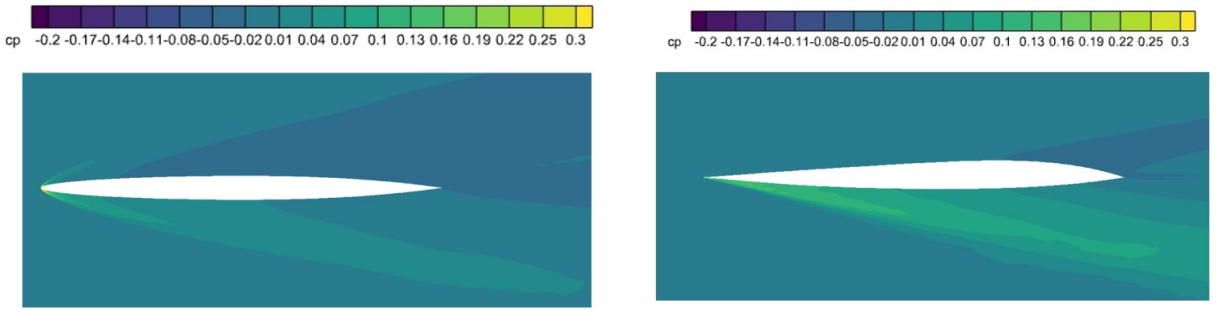

Figure 24. Pressure coefficient variation chart ((**left**) baseline, (**right**) optimized).

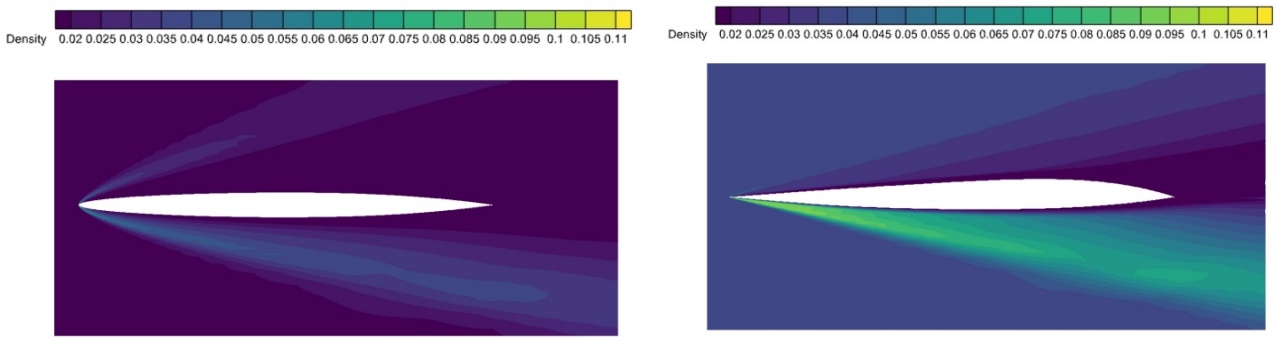

Figure 25. Density variation chart ((**left**) baseline, (**right**) optimized).

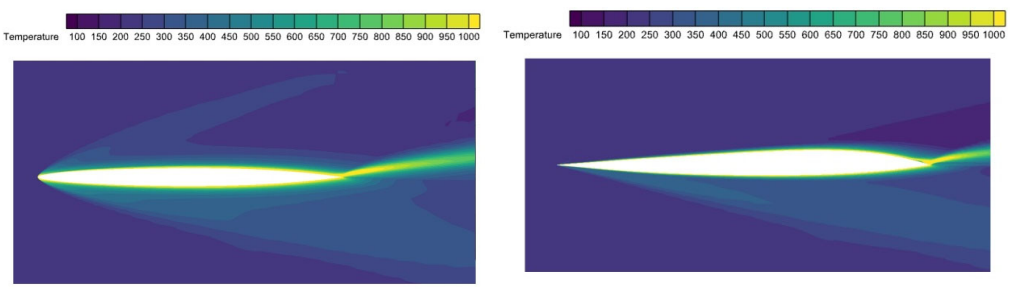

Figure 26. Temperature variation chart ((**left**) baseline, (**right**) optimized).

Table 4 lists the values of the drag coefficient, lift coefficient, moment coefficient, and wing area before and after optimization. It can be observed that the drag coefficient decreased from 0.025 to 0.015, a reduction of 40%, while the lift coefficient, moment coefficient, and wing area remained unchanged. Consequently, the lift-to-drag ratio increased, from 3.28 to 5.47, indicating a significant improvement in aerodynamic performance. These results demonstrate the effectiveness of the optimization.

Table 4. Comparison of aerodynamic parameters before and after optimization.

Parameter	C_D	C_L	C_m	A_m
baseline	0.025	0.082	−0.012	0.043855
optimization	0.015	0.082	−0.012	0.043855

5. Conclusions

This study systematically reviews the developmental trajectory of high-speed vehicles in domestic and international contexts, with particular emphasis on the SR-72 program. Through comprehensive analysis of declassified U.S. project documentation, a three-dimensional SR-72 model was reconstructed using publicly available schematics, followed by detailed structured mesh generation and computational fluid dynamics (CFD) simulations. Key aerodynamic findings are summarized as follows:

(1) Subsonic Regime

The configuration demonstrated superior maneuverability with an extended stall angle of attack (24°), fulfilling fundamental requirements for high-g maneuvers. Progressive development of negative pressure belts along the upper fuselage surface was observed with increasing angles of attack. Maximum lift-to-drag ratio (L/D) occurred at 4° angle of attack, indicating optimal aerodynamic efficiency.

(2) Transonic Regime

Significant wave drag characteristics were identified near Mach 1, accompanied by complex surface flow structures and reduced L/D ratios ($\leq$2.8). This regime exhibited critical aerodynamic instabilities, necessitating dedicated flight control strategies.

(3) Supersonic Regime

Computational analysis at Mach 2–3 revealed enhanced aerodynamic efficiency and heightened sensitivity to angle-of-attack variations. The configuration achieved peak L/D ratios approaching 4.6, demonstrating exceptional supersonic performance.

(4) High-Mach-number Regime

The vehicle exhibited superior high-Mach-number capabilities with maximum L/D ratios approaching 5.0. Flow field visualization confirmed significant pressure differentials between upper and lower surfaces, where the wave-rider body configuration generated substantial compression lift. This aerodynamic design enables extended cruise endurance with minimized fuel consumption.

(5) Optimization

A high-speed airfoil optimization framework was developed. Under the conditions of Mach 6 and a 6-degree angle of attack, the NACA 16006 airfoil was optimized using the Sequential Least Squares Programming (SLSQP) method. While satisfying the constraints on lift coefficient, moment coefficient, and wing area, the drag coefficient was successfully reduced from 0.025 to 0.015, achieving a 58% improvement in lift-to-drag ratio and a significant enhancement in aerodynamic performance.

This paper analyzes the aerodynamic characteristics of a high-speed vehicle, presenting computational analyses for four Mach number ranges and providing reference results for subsequent engineering use. Finally, the wing is optimized and an optimization framework is developed that is applicable to standard NACA airfoils, laying a foundation

for practical applications. When selecting a wing in engineering projects, the optimization framework proposed here can be used for preliminary tuning. The above summarizes how this paper can assist in engineering work.

Author Contributions: Conceptualization, C.F. and F.H.; methodology, C.F. and F.H.; software, G.C. and L.Z.; validation, G.C., F.H., C.F. and B.D.; formal analysis, C.F.; investigation, C.F. and B.D.; resources, C.F., J.L. and L.Z.; data curation, L.Z.; writing, C.F.; visualization, L.Z. and J.L.; supervision, J.L. and C.F.; project administration, C.F, B.D. and J.L.; funding acquisition, J.L. and L.Z. All authors have read and agreed to the published version of the manuscript.

Funding: Defense Industrial Technology Development Program (No. JCKY2023205B013) the National Natural Science Foundation of China (NO. U2241274) Supported by the specialized research projects of Huanjiang Laboratory.

Data Availability Statement: The original contributions presented in this study are included in the article. Further inquiries can be directed to the corresponding authors.

Conflicts of Interest: The authors declare no conflicts of interest.

Abbreviations

The following abbreviations are used in this manuscript:

NACA	National Advisory Committee for Aeronautics
CST	Class-Shape Transformation
SLSQP	Sequential Least Squares Programming
UVA	Unmanned Aerial Vehicle
RBCC	Rocket-Based Combined Cycle
TBCC	Turbine-Based Combined Cycle
CFD	computational fluid dynamics
AoA	Angle of Attack

References

1. War Thunder Forum. (22 September 2023). MiG-25 & MiG-31 Foxbat/Foxhound—History, Design, Performance Dissection. Available online: https://toad-design.com/migalley/index.php/jet-aircraft/mig25/ (accessed on 5 August 2024).
2. Wikipedia Contributors. Mikoyan-Gurevich MiG-25. Available online: https://en.wikipedia.org/w/index.php?title=Mikoyan-Gurevich_MiG-25&oldid=1311810106 (accessed on 22 September 2025).
3. Liu, T.L. Russia's hypersonic technology flight test program (Part 3). *Aerodyn. Missile J.* **2000**, *6*, 17–23. (In Chinese)
4. Wikipedia Contributors. Tupolev PAK DA. Available online: https://en.wikipedia.org/w/index.php?title=Tupolev_PAK_DA&oldid=1296211375 (accessed on 22 September 2025).
5. Luo, S.; Sun, Y.; Liu, J.; Xie, X.; Tian, J.; Song, J. Research status and development trend of air-breathing high-speed vehicle/engine integration. *Aerosp. Sci. Technol.* **2024**, *155*, 109675. [CrossRef]
6. Dryden Flight Research Center. XB-70, National Aeronautics and Space Adiministration, NASA Facts. Available online: https://www.nasa.gov/wp-content/uploads/2021/09/121584main_fs-084-dfrc.pdf (accessed on 1 August 2024).
7. Chase, R.; Tang, M. A history of the NASP Program from the formation of the Joint Program Office to the termination of the HySTP Scramjet Performance Demonstration Program. In *International Aerospace Planes and Hypersonics Technologies*; AIAA: Reston, VA, USA, 1995.
8. AIAA. The Hyper-X Launch Vehicle: Challenges and Design Considerations for Hypersonic Flight Testing. In *Proceedings of the AIAA/CIRA 13th International Space Planes and Hypersonics Systems and Technologies Conference*; AIAA: Reston, VA, USA, 2005.
9. Wikipedia Contributors. NASA X-43. Available online: https://en.wikipedia.org/w/index.php?title=NASA_X-43&oldid=1297814493 (accessed on 22 September 2025).
10. Voland, R.T.; Huebner, L.D.; Mcclinton, C.R. X-43 Hypersonic Vehicle Technology Development. *Acta Astronautica* **2006**, *59*, 181–191. [CrossRef]
11. Harsha, P.; Keel, L.; Castrogiovanni, A.; Sherrill, R. X-43A Vehicle Design and Manufacture. In Proceedings of the AIAA/CIRA 13th International Space Planes and Hypersonics Systems and Technologies Conference, Capua, Italy, 16–20 May 2005. Available online: https://www.semanticscholar.org/paper/X-43-Hypersonic-Vehicle-Technology-Development-Voland-Huebner/f6df12260f7c53e92fa017339a41809eb4ab03c6 (accessed on 1 August 2024).

12. Powell, O.A.; Edwards, J.T.; Norris, R.B.; Numbers, K.E.; Pearce, J.A. Development of Hydrocarbon-Fueled Scramjet Engines: The Hypersonic Technology (HyTech) Program. *J. Propuls. Power* **2001**, *17*, 1170–1176. [CrossRef]
13. Lux-Baumann, J.; Burkes, D.A. Hyper-X (X-43A) flight test range operations overview. In Proceedings of the Aerospace Testing Expo, Anaheim, CA, USA, 14–16 November 2006.
14. Hank, J.; Murphy, J.; Mutzman, R. The X-51A Scramjet Engine Flight Demonstration Program. In Proceedings of the 15th AIAA International Space Planes and Hypersonic Systems and Technologies Conference, Dayton, OH, USA, 28 April–1 May 2008.
15. Hank, J.; Murphy, J.; Mutzman, R. X-51A Scramjet Engine Flight Demonstration Program. *AIAA J. Propuls. Power* **2012**, *28*, 733–746.
16. Christopher, M.; Rondeau, M. X-51A Scramjet Demonstrator Program: Waverider Ground and Flight Test. In Proceedings of the SFTE 44th International/SETP Southwest Flight Test Symposium, Ft Worth, TX, USA, 28 October–1 November 2013.
17. McClinton, C.R. Hypersonic WaveRider technology: Lessons from the X-51A. In *AIAA Scitech Forum*; American Institute of Aeronautics and Astronautics: Reston, VA, USA, 2007. [CrossRef]
18. Heiser, W.H.; Pratt, D.T. Hypersonic airbreathing propulsion: The X-51A and beyond. *Annu. Rev. Fluid Mech.* **2018**, *50*, 591–614. [CrossRef]
19. Hofmann, J.P.; Stumpf, E.; Werner, E.A. A Comprehensive Approach to the Assessment of a Hybrid Electric Powertrain for Commuter Aircraft. In Proceedings of the AIAA Aviation Forum and Exposition, Dallas, TX, USA, 17–21 June 2019.
20. Abdelmalek, M.F.; Charles, E.D.; Sanyal, A.J.; Harrison, S.A.; Neuschwander-Tetri, B.A.; Goodman, Z.; Ehman, R.A.; Karsdal, M.; Nakajima, A.; Du, S.; et al. The FALCON program: Two phase 2b randomized, double-blind, placebo-controlled studies to assess the efficacy and safety of pegbelfermin in the treatment of patients with nonalcoholic steatohepatitis and bridging fibrosis or compensated cirrhosis. *Contemp. Clin. Trials* **2021**, *104*, 106335. [CrossRef]
21. De Bari, B.; Dahele, M.; Palmu, M.; Kaylor, S.; Schiappacasse, L.; Guckenberger, M. Short interactive workshops reduce variability in contouring treatment volumes for spine stereotactic body radiation therapy: Experience with the ESTRO FALCON programme and EduCase™ training tool. *Radiother. Oncol.* **2018**, *127*, 150–153. [CrossRef] [PubMed]
22. Kim, H.S.; Yang, W.S.; Choi, J.Y. Sub-Orbital Hypersonic Flight Test Programs using Sounding Rockets and Small Launch Vehicles. *J. Korean Soc. Aeronaut. Space Sci.* **2015**, *43*, 243–256. [CrossRef]
23. Lei, Q.; Li, J.L.; Zhao, D. Tracking Filter and Prediction for Non-ballistic Target HTV-2 in Near Space. In *Qingdao, Shandong, China*; IEEE: New York, NY, USA, 2015.
24. Shao, C.; Nie, L.; Chen, W. Analysis of electromagnetic scattering characteristics for an HTV-2 type flight vehicle ablation flows. In Proceedings of the 29th International Symposium on Rarefied Gas Dynamics, Xi'an, Shaanxi, China, 13–18 July 2014.
25. Walker, S.; Tang, M.; Morris, S.; Mamplata, C. Falcon HTV-3X—A Reusable Hypersonic Test Bed. In Proceedings of the 15th AIAA International Space Planes and Hypersonic Systems and Technologies Conference (AIAA), Dayton, OH, USA, 28 April–1 May 2008.
26. Boudreau, A.H. Status of the U.S. Air Force HYTECH Program. AIAA Paper 2011. Available online: https://arc.aiaa.org/doi/10.2514/6.2003-6947 (accessed on 1 August 2024).
27. Yun, W. Starry Sky-2 rocket: Achieving the first domestic waverider flight. *Space Explor.* **2018**, *9*, 5. (In Chinese)
28. Global Space Dynamics. *Int. Space* **2019**, *5*, 56–58. Available online: https://baike.baidu.com/item/%E5%8E%A6%E5%A4%A7%E5%98%89%E5%BA%9A%E4%B8%80%E5%8F%B7%E7%81%AB%E7%AE%AD/63078393 (accessed on 1 August 2024). (In Chinese)
29. Norris, G. Skunk Works reveals SR-71 successor plan. *Int. Aviat.* **2013**, *11*, 3. (In Chinese)
30. Wikipedia Contributors. Lockheed Martin SR-72. Available online: https://en.wikipedia.org/w/index.php?title=Lockheed_Martin_SR-72&oldid=1311601131 (accessed on 22 September 2025).
31. Xiao, B.U.S. "Son of Blackbird" SR-72 plan exposed. *Sci. Grandview* **2014**, *7*, 81. (In Chinese)
32. Guo, Y.C. Three-Dimensional Reconstruction and Aerodynamic Characteristics Analysis of SR-72 Hypersonic Unmanned Reconnaissance Aircraft. Master's Thesis, Nanjing University of Aeronautics and Astronautics, Nanjing, China, 2016. (In Chinese)
33. Wieting, A.R. *Experimental Study of Shock Wave Interference Heating on a Cylindrical Leading Edge*; NASA Langley Research Center: Hampton, VA, USA, 1987.
34. Anderson, J.D., Jr. *Fundamentals of Aerodynamics*, 6th ed.; McGraw-Hill Education: Columbus, OH, USA, 2017.
35. Roache, P.J. Perspective: A Method for Uniform Reporting of Grid Refinement Studies. *J. Fluids Eng.* **1994**, *116*, 405–413. [CrossRef]
36. Kulfan, B.; Bussoletti, J. 'Fundamental' Parameteric Geometry Representations for Aircraft Component Shapes. In Proceedings of the 11th AIAA/ISSMO Multidisciplinary Analysis and Optimization Conference, Portsmouth, VA, USA, 6–8 September 2006.